

IMMEDIATE ONLINE ACCEPTED (IOA) ARTICLE

This article presented here has been peer reviewed and accepted for publication in *CCS Chemistry*. The present version of this manuscript has been posted at the request of the author prior to copyediting and composition and will be replaced by the final published version once it is completed. The DOI will remain unchanged.

IOA Posting Date: November 13, 2020

TITLE: Synthesis of iron carbide nanoparticles: Identification of the active phase and mechanism of Fe-based Fischer-Tropsch Synthesis

AUTHORS: Huabo Zhao, Jin-Xun Liu, Ce Yang, Siyu Yao, Hai-Yan Su, Zirui Gao, Mei Dong, Jianguo Wang, Yanglong Hou, Wei-Xue Li and Ding Ma

DOI: 10.31635/ccschem.020.202000555

Synthesis of iron carbide nanoparticles: Identification of the active phase and mechanism of Fe-based Fischer-Tropsch Synthesis

Huabo Zhao^{1‡}, Jin-Xun Liu^{2‡}, Ce Yang^{3‡}, Siyu Yao¹, Hai-Yan Su⁴, Zirui Gao¹, Mei Dong⁵, Jianguo Wang⁵, Yanglong Hou^{3*}, Wei-Xue Li^{2*} and Ding Ma^{1*}

¹ College of Chemistry and Molecular Engineering, Peking University, Beijing, 100871

² Department of Chemical Physics, School of Chemistry and Materials Science, Hefei National Laboratory for Physical Science at the Microscale, iCHEM, University of Science and Technology of China, Hefei 230026

³ Department of Materials Science and Engineering, College of Engineering, Peking University, Beijing 100871

⁴ School of Chemical Engineering and Energy Technology, Dongguan University of Technology, Dongguan 523808

⁵ State Key Laboratory of Coal Conversion, Institute of Coal Chemistry, Chinese Academy of Sciences, Taiyuan 030001

*Corresponding Author(s): Yanglong Hou: hou@pku.edu.cn; Wei-Xue Li: wxli70@ustc.edu.cn; Ding Ma: dma@pku.edu.cn

‡These authors contributed equally.

Abstract

Despite the extensive study of Fe-based Fischer-Tropsch synthesis (FTS) over the past 90 years, its active phases as well as the reaction mechanisms are still unclear due to the co-existence of metals, oxides and carbide phases presented under realistic FTS reaction conditions and the complex reaction network involving CO activation, C-C coupling and methane formation. To address this issue, we successfully synthesized a range of pure phase iron and iron carbide nanoparticles (Fe, Fe₅C₂, Fe₃C,

Fe₇C₃) for the first time. By using them as the ideal model catalysts on high-pressure transient experiments, we identified unambiguously that all the iron carbides are catalytically active in FTS reaction while Fe₅C₂ is the most active yet stable carbide phase, which is consistent with density functional theory (DFT) calculation results. The reaction mechanism and kinetics of Fe-based FTS was further explored on the basis of those model catalysts by means of transient high-pressure stepwise temperature-program surface reaction (STPSR) experiment and DFT calculations. Our work provides new insights into the active phase of iron carbides and corresponding FTS reaction mechanism, which is essential for better iron-based catalysts design for FTS reaction.

Keywords

Fischer-Tropsch synthesis, iron carbides, active phase, mechanism

Introduction

Fischer-Tropsch synthesis (FTS) receives increasing attention because synthesis gas (syngas) can be obtained from coal, biomass and shale gas, which becomes particularly importance as alternative fuel and chemicals production.¹⁻² Despite the extensive exploration of Fe-based catalysts over the past 90 years, its active phases and reaction mechanisms are still in controversial.³ The typical iron catalysts, usually produced from thermal reduction and successive activation of iron oxide precursors, contain different phases including metals, oxides and carbides produced during the pretreatment of the catalysts by carbon-containing gases such as CO.⁴⁻¹⁰ The phase evolution of the iron catalysts during FTS reaction is even more complicated, and in most cases, a mixture of different phases was resulted during the FTS reaction.¹¹⁻¹⁵ To address this issue, various types of metal or metal carbides were prepared.¹⁶⁻²² Metallic iron,²³⁻²⁴ and various phases of iron carbides had all been claimed to be active.^{4, 6, 25-38} The complication for FTS comes also from the complexity of the reaction network itself, including CO activation, C-C bond formation and methane formation.^{32, 39-45} However, the reaction

performance dependence on catalyst phases of iron and carbides as well as the catalytic mechanism behind was still elusive, which hinders better Fe-based catalyst design for FTS.

To address these challenging issues, we have successfully, for the first time, synthesized a variety of pure phase iron and iron carbide catalysts with similar particle size, including Fe, Fe₇C₃, Fe₃C, Fe₅C₂, etc., which allow us to identify their initial and intrinsic activities as well as the structural evolutions of iron-based catalysts during FTS. At the same time, we developed a new transient experiment, i.e., transient high-pressure stepwise temperature-program surface reaction (STPSR), which enables us to explore directly the complicated yet challenging problems in FTS such as the fundamental knowledge about syngas activation, hydrocarbon and methane formation on these pure phase catalysts, which were not available before. The comprehensive density functional theory (DFT) calculations revealed a deep insight on the intrinsic activity of iron metal and iron carbides on CO activation, C-C bond and methane formation, rationalizing the kinetic and thermodynamic origin on the structural evolution of different iron-based catalysts during the FTS reaction. The deeper understanding the active phase of iron-based catalysts and corresponding FTS reaction mechanism is beneficial for rational design of more effective Fe-based catalysts on FTS by the synthesis of more Fe₅C₂ catalyst.

Experimental Methods

Synthesis of Fe₇C₃ and Fe₂C NPs

In a four-neck flask, 20 mL of N,N-dimethyloctadecylamine (for Fe₇C₃) or dodecylamine (for Fe₂C) was stirred sufficiently and degassed under 120 °C for 2 h. Then, the system was refilled with NH₃ and heated to 180 °C. After that, Fe(CO)₅ (0.7 mL, 5.0 mmol) was injected under NH₃ atmosphere and kept at this temperature for 30 min. A colour change from orange to black was observed during the process, implying the decomposition of Fe(CO)₅ and the nucleation of Fe nanocrystals. Subsequently, the mixture was further heated to 350 °C (for Fe₇C₃) or 260 °C (for Fe₂C) at 10 °C /min and kept for 2

h before it was cooled down to room temperature. The product was washed with ethanol and hexane, and collected for further characterization. The as-synthesized NPs were kept in Ar-filled glove box to avoid exposure to air before further characterization. In the absence of NH_3 , the nanoparticles (NPs) would be oxidized to iron oxide (Fig S1 and Fig. S2).

Synthesis of Fe_5C_2 and Fe NPs

In a four-neck flask, a mixture of octadecylamine (14.5 g) and CTAB (0.113 g) was stirred sufficiently. Then, the system was refilled with N_2 and heated to 180 °C. Following that, $\text{Fe}(\text{CO})_5$ (0.5 mL, 3.6 mmol) was injected under a N_2 blanket. The mixture was kept at 180 °C for 10 min. A color change from orange to black was observed during the process, implying the decomposition of $\text{Fe}(\text{CO})_5$ and the nucleation of Fe nanocrystals. Subsequently, the mixture was further heated to 350 °C (for Fe_5C_2) or 300 °C (for Fe) at 10 °C /min and kept for 10 min before it was cooled down to room temperature. The product was washed with ethanol and hexane, and was kept in Ar-filled glove box to avoid exposure to air before further characterization.

Preparation of supported catalyst

The NPs obtained from high temperature liquid phase synthesis had been washed with n-hexane and ethanol for several times and dispersed in n-hexane under N_2 protection. After, the dispersion of iron carbide NPs was added into a certain amount of silica (N_2 adsorption-desorption isotherm was shown in Fig. S3) under stirring. After evaporating the solvent at room temperature, the supported catalyst was prepared. The amount of iron determined by ICP was around 8%.

Catalysis Reaction:

The catalytic performance of the catalysts was evaluated in a fixed bed reactor. 80 mg catalyst was loaded in a quartz-lining stainless steel reactor. The feed gas was a mixture of 32% CO , 64% H_2 and 4% Ar. In a typical reaction, the pressure and gas flow rate was set for 30 bar and 20 mL/min

(GHSV=15000 mL·g⁻¹·h⁻¹) respectively. Then, the reaction tube was heated from room temperature to 270 °C at 5 °C /min, and the reaction was conducted at 270 °C. It is worth noting that no reduction or carburizing pretreatment was carried out before reaction. The gas phase products were analyzed by an Agilent 6890 GC equipped with an FID and TCD detector, with 4% Ar as inert standard. The heavier hydrocarbons were cooled down and collected in a trap, and analyzed offline by an Agilent GC 7820, with a HP-5 capillary column and FID detector. The products selectivity was calculated on a carbon basis.

STPSR Experiment

Prior to the STPSR experiments, the Fe catalyst was treated in H₂ (20 mL/min) and the Fe₅C₂ catalyst was treated in 10% C₂H₄/H₂ mixture at 300 °C for 2 hrs to remove the surface contaminates. After cooling down to RT, the gas flow was switched to synthesis gas of 20 mL/min and the pressure was raised to 30 bar. Then, the reactor was heated to 150 °C at 20 °C /min, and kept steady for 2 hrs. Afterward, the temperature was elevated 20 °C higher and held for 2 hrs at that temperature. The process was repeated until the reaction temperature reached 270 °C. A Pfeiffer mass spectrometer (MS) Omnistar was used to analyze on-line the reactants and products. The M/e value detected as follows: 2 for hydrogen, 15 for methane, 18 for water, 26, 27, 30 for C₂ products (acetylene, ethylene, and ethane), 28 for CO, 42 for C₃, 44 for CO₂, 56 for C₄⁺ and 70 for C₅⁺.

Catalyst Characterization

The TEM experiments were conducted at a FEI Tecnai F30 transmission electron microscope operating at 300 keV. The XPS experiments were carried out in an Axis Ultra imaging photo electron spectrometer with Al K α as X-ray source. The binding energy of graphite carbon was calibrated to 284.8 eV. X-ray powder diffraction data were collected at a Rigaku DMAX-2400 equipped with Cu Al K α radiation. The Raman characterizations were performed on a Renishaw 1000 Raman imaging microscope system with an excitation wavelength of 632.8 nm. The ⁵⁷Fe Mössbauer Effect spectra of

as-synthesized iron carbide NPs were collected by a Topological 500A spectrometer and a proportional counter at room temperature. The γ radiative source was a ^{57}Co (Rh) moving with constant acceleration mode. The XAFS spectra were collected at beam line 14W of Shanghai Synchrotron Facility (SSRF) in transmission mode with Si (111) monochromator. The samples for characterization were prepared and transferred under protection of Ar. As metallic iron and iron carbide were very sensitive for oxidation, sometimes the oxidation of the sample is unavoidable. For TEM study, the used catalyst was passivated in 0.5% O_2 in Ar at room temperature for 1 hr before the measurement.

Calculation

Spin-polarized DFT calculations have been performed by using Vienna Ab Initio Simulation Package (VASP).⁴⁶⁻⁴⁷ Throughout the calculations, projector augmented wave (PAW) potential⁴⁸ and the generalized gradient approximation (GGA) with the Perdew–Burke–Ernzerhof (PBE) exchange–correlation functional⁴⁹ was adopted. The planewave cutoff energy was set by 400 eV. The force and energy convergence standards were 0.02 eV/Å and 1×10^{-4} eV, respectively. Monkhorst–Pack⁵⁰ k-points sampling of $3 \times 7 \times 7$ and $10 \times 10 \times 10$ were adopted for Fe_5C_2 and Fe bulk calculations with monoclinic (space group C2/c) and body centered cubic (BCC) crystal structures, respectively. The optimized lattice constant of Fe_5C_2 is $a=11.55$ Å, $b=4.50$ Å and $c=4.99$ Å with $\beta=97.6^\circ$, which are consistent with experimental findings that $a=11.59$ Å, $b=4.58$ Å and $c=5.06$ Å with $\beta=97.75^\circ$.⁵¹ The determined lattice constant (2.83 Å) for Fe with body centered cubic (BCC) crystal structure also agrees very well with experiment.⁵²

Fe-terminated Fe_5C_2 (100) surface was simulated by a slab of seven-layered Fe atoms and three-layered C atoms. In the calculations, the topmost four Fe and one C layers were fully relaxed, whereas the remained atoms were fixed in their bulk positions. For BCC-Fe (310) surface, ten Fe atoms layered slab model was used, and only the top five Fe layers are allowed to relax. A $p(2 \times 2)$ unit

cell was utilized for the two considered slab models. We have used Monkhorst–Pack mesh k-points of $3 \times 3 \times 1$ for Fe_5C_2 (100), and $5 \times 5 \times 1$ for BCC-Fe (310) surface. The vacuum region along the z direction was specified by 15 Å, and the dipole correction was considered in our calculations. Force-reversed method⁵³ was used to locate the transition states (TSs) and a force tolerance of 0.03 eV/Å was applied without zero-point correction. Some TSs along the minimum-energy reaction pathways were also reaffirmed by using the climbing image nudged elastic band (CI-NEB) method.⁵⁴ For a given elementary reaction, we considered the separately adsorption of intermediates at their most favourable adsorption sites as the initial and final states for the reaction barriers calculations.

Results and Discussion

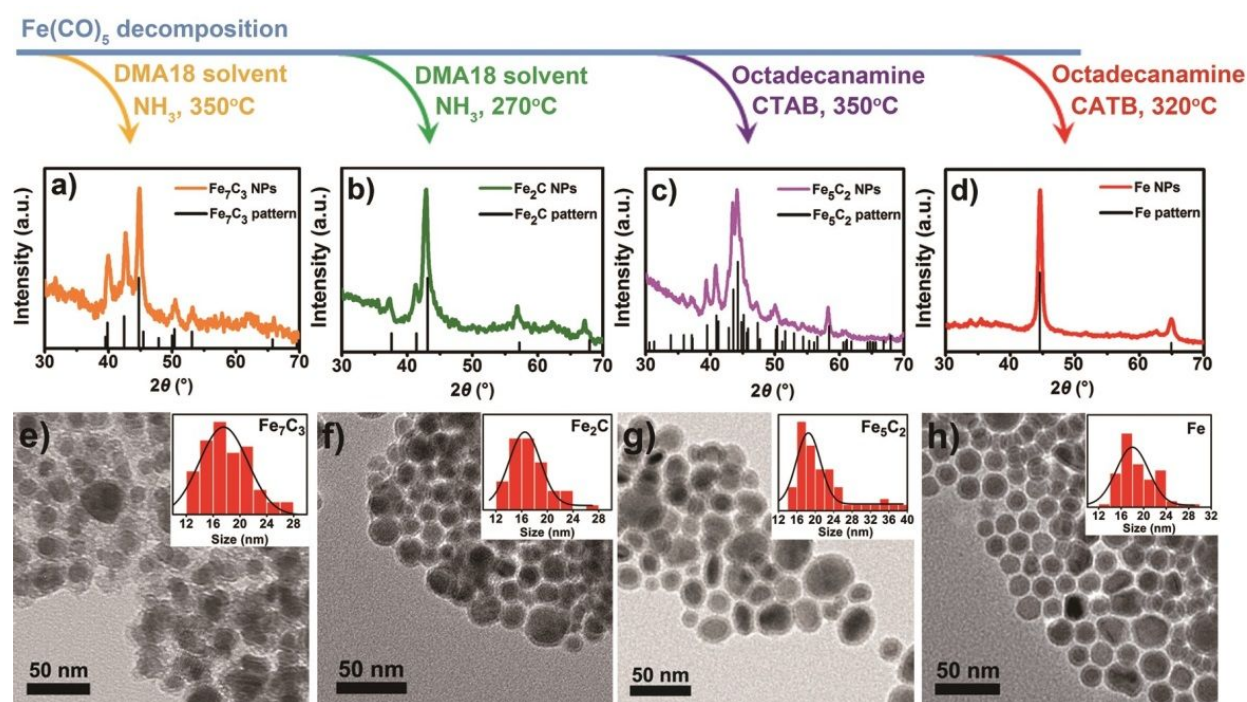


Fig. 1. XRD patterns and TEM images of Fe_7C_3 (a, e), Fe_2C (b, f), Fe_5C_2 (c, g) and $\alpha\text{-Fe}$ (d, h) NPs. It is clear from the TEM images and XRD profiles that all the obtained Fe and iron carbide nanoparticles have the pure phase structure and similar size (around 18 nm).

In fabrication of both Fe_7C_3 and Fe_2C NPs, NH_3 was chosen as atmosphere as well as inducing agent while $\text{Fe}(\text{CO})_5$ was used as precursor. In particular, Fe_7C_3 NPs were obtained in *N,N*-dimethyloctadecylamine solvent under 350 °C for 2 h and Fe_2C NPs were produced in dodecylamine solvent under 260 °C for 2 h (see Supporting Information). α -Fe and Fe_5C_2 NPs were synthesized via a bromide-induced process as described elsewhere.¹⁹ Fig. 1 presented the X-ray Powder Diffraction (XRD) patterns and corresponding transition electron microscope (TEM) images of as-synthesized Fe_7C_3 , Fe_2C , Fe_5C_2 and α -Fe NPs. According to the XRD results, the peaks in each sample were in good consistence with the standard patterns, which suggests the generation of single phase in each of the four samples. Furthermore, TEM images of the four samples indicate that they are all spherical NPs with size around 18 nm.

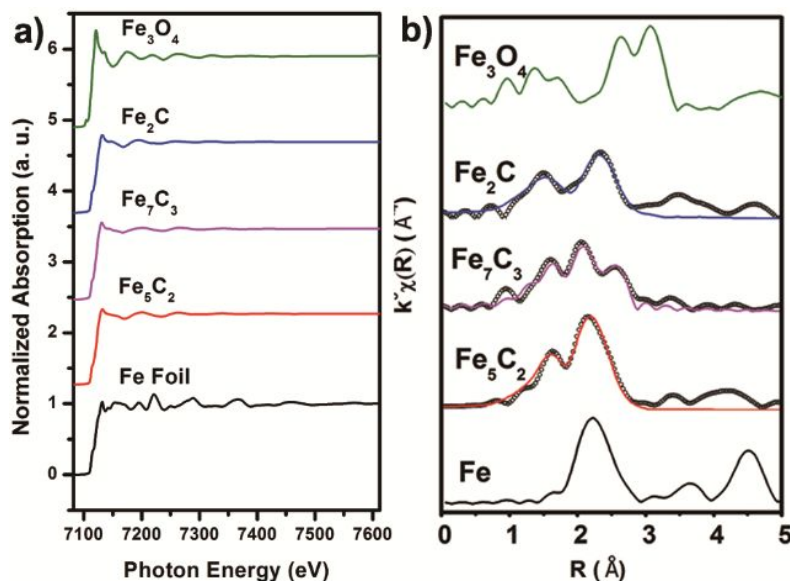


Fig. 2. a) XANES and b) EXAFS spectra of Fe_5C_2 , Fe_7C_3 and Fe_2C . The XANES and EXAFS spectra of Fe foil and standard pattern of Fe_3O_4 are shown by black curve and green curve, respectively. The curves composed by black circles in b) indicate the experimental data of each iron carbide and the colored curves indicate the simulation curves. The XAFS samples were prepared and transferred under protection of Ar.

The X-ray Absorption Fine Structure (XAFS) and Mössbauer spectra data also support this conclusion. Fe K edge XANES suggests that the iron carbide particles exhibit very low oxidation state as compared to the metallic Fe foil. The relatively low frequency oscillation of the post-edge features indicates Fe central atom has neighbours with small bond length. Further EXAFS fitting results confirm that all of the Fe carbide particles synthesized have Fe-C coordination shell near 2.0 Å, the average first Fe-Fe shell bond length expands from 2.46 Å to around 2.60 Å, due to the incorporation of carbon into the BCC lattice of α -Fe (Fig. 2). Furthermore, no features of Fe oxides and Fe are observed, suggesting all the particles are pure carbide. Moreover, the Mössbauer spectra have been shown in Fig. S4. The sextet peaks indicates the formation of Fe_2C , Fe_7C_3 and Fe_5C_2 NPs, while the weak doublet peaks in Fe_5C_2 suggests that the Fe_5C_2 NPs may have better crystallinity compare with Fe_2C and Fe_7C_3 . Therefore, single-phase nature of these α -Fe and iron carbide NPs along with their similar morphology provide us with ideal platforms for the investigation of their intrinsic catalytic behavior and structural evolution in FTS process. At the same time, as the cementite (Fe_3C) was reported to have poor activity in FTS,^{30, 32} it is not discussed in this work.

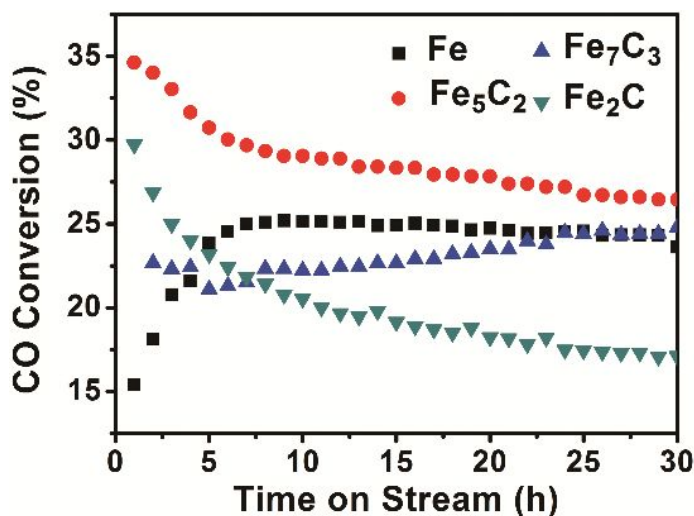


Fig. 3. CO conversion as a function of time over Fe, Fe_2C , Fe_7C_3 and Fe_5C_2 catalysts (reaction conditions: 270 °C, 30 bar, 20 ml/min syngas).

The α -Fe and iron carbide NPs were dispersed on silica support and directly used in FTS reaction (3 MPa syngas, 270 °C). For a 40 h reaction, the product distribution on Fe and Fe₅C₂ are similar except Fe has a higher C₅₊ selectivity (49%). Fe₂C has the highest selectivity towards CO₂ (22.7%), while Fe₂C and Fe₇C₃ show considerably high selectivity of 20.1% and 19.5% toward methane, respectively (Fig. S5). Both CO₂ and CH₄ are undesired products. CO conversion on prepared catalysts with time on stream is shown in Fig. 3 with FTS activity shown in Table 1.

Table 1. The surface-specific activity (TOF) and metal-mass-based activity (Activity) excluded CO₂ formation over various iron and iron carbides catalysts.

Catalysts	Temperature (°C)	Pressure (bar)	TOS (h)	TOF _{FTS} (s ⁻¹)	Activity (1×10 ⁻⁴ Mol _{CO} .g _{Fe} ⁻¹ .s ⁻¹)	Reference
Fe	270	30	1	0.13	1.1	This work
Fe	270	30	30	0.20	1.7	This work
Fe ₅ C ₂	270	30	1	0.29	2.3	This work
Fe ₅ C ₂	270	30	30	0.22	1.8	This work
Fe ₇ C ₃	270	30	1	0.16	1.6	This work
Fe ₇ C ₃	270	30	30	0.18	1.7	This work
Fe ₂ C	270	30	1	0.16	1.8	This work
Fe ₂ C	270	30	30	0.09	1.0	This work
Fe _x O _y @C	270	20	-	-	0.31	55
Fe/SiO ₂	270	20	-	-	0.20	56
Fe-in-CNT	270	50	-	-	2.5	57
25-Fe@C	340	20	-	0.11	4.9	58
RQ Fe	200	30	-	-	3.5	59

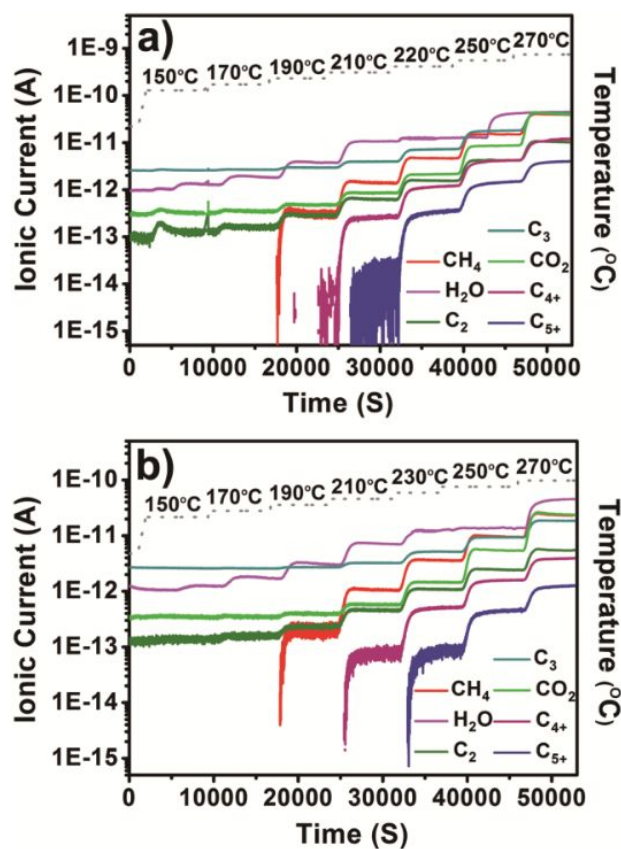


Fig. 4. STPSR profile on Fe_5C_2 (a) and Fe (b) catalysts.

At the beginning, Fe_5C_2 exhibits the highest CO conversion (around 35%), followed by Fe_2C (29.5%) and Fe_7C_3 (22.5%), while $\alpha\text{-Fe}$ had the lowest CO conversion (15.2%). The initial CO reactivity reflects the intrinsic catalytic properties of Fe_2C , Fe_7C_3 and Fe_5C_2 . With the reaction proceeding, the activities of the four catalysts showed different trends. For Fe_5C_2 and Fe_2C , the CO conversion decreased sharply in the first 6 hrs but gradually stabilized later on. For Fe_7C_3 , CO conversion dropped slightly in the first 5 hrs, after a small increase, became stabilized. On the contrary, that of $\alpha\text{-Fe}$ catalyst increased rapidly in the first 7 hrs, and then remained almost constant afterwards. When the conversion for all catalysts approached the steady state, Fe_5C_2 remains the most active one with a conversion of 27%, and the activities of Fe_7C_3 and Fe (25% and 24%) are slightly lower, whereas Fe_2C becomes the least active one (17%). The TOF and activity of those Fe-based catalysts were summarized in table 1. Obviously, Fe_5C_2 has the highest initial and steady state activities (2.3 and 1.8

$\times 10^{-4} \text{ Mol}_{\text{CO}} \cdot \text{g}_{\text{Fe}}^{-1} \cdot \text{s}^{-1}$). After reaction, the morphologies of used Fe_5C_2 and Fe_2C catalysts were maintained with main phases transformed into a mixture of iron oxide and original carbide, whereas for Fe_7C_3 , the formation of Fe_5C_2 was observed (Fig. S6 and S7). Significantly, the main phase of used $\alpha\text{-Fe}$ catalyst was transformed into Fe_5C_2 , in addition to Fe_3O_4 (Fig. S6). There has always been a debate on whether and why metal and/or carbide is the active phase for FTS. To examine this, we chose Fe_5C_2 as a representative for carbide phase and compared its catalytic behavior in the early stage of FTS with that of $\alpha\text{-Fe}$ catalyst. We designed a high-pressure stepwise temperature programming surface reaction (STPSR) apparatus, to allow the observation of reaction kinetics at high pressure. This TPSR experiment enables the observation of those masked information by steady-state reaction evaluation.^{17, 60-61}

The formation of various products during the STPRS of syngas over the Fe_5C_2 catalyst is illustrated in Fig. 4a. Before 150 °C, no products were formed, which indicates that syngas cannot be activated over Fe_5C_2 at temperatures below 150 °C. With the reaction temperature reaching 150 °C and remaining for 20 min, the formation of water, C_2 hydrocarbons (mostly acetylene and ethylene) and CO_2 were observed. When the temperature was raised to 170 °C, with the appearance of C_3 hydrocarbon, the amount of water and C_2 formed were considerably high. Yet, to our surprise, methane was not detected until then. The MS signal for methane appeared only when the reaction temperature reached 190 °C. The formation of methane at higher temperature than that of C_2 hydrocarbons indicates that the hydrogenation of monomers toward methane is kinetically less favorable than C-C coupling. When the temperature reached 210 °C, C_4 compounds appear, followed with the formation of C_{5+} hydrocarbons until 20 min later.

To our surprise, STPSR profile of $\alpha\text{-Fe}$ catalyst shows a distinct behavior as compared with that of Fe_5C_2 (Fig. 4b). At 150 °C, water formation was reproducibly observed, whereas no C_2 hydrocarbons could be detected in 2 hrs. Instead, C_2 hydrocarbon appeared only at around 10 min after the temperature reaching 170 °C. The formation temperature of methane, C_3 alkane, and CO_2

was at least 190 °C. C₄ and C₅ formed at 210 °C and 230 °C, which are very similar to those of Fe₅C₂. Thus, although C₂ hydrocarbon on α-Fe formed at a higher temperature (170 °C) than that on Fe₅C₂ (150 °C), the formation of methane on both catalysts requires a temperature of 190 °C or higher. Namely, methane formation on both catalysts remains less favorable, compared with the formation of water and C₂ hydrocarbon. The formation of water in STPSR process is interesting as the pre-adsorbed water on the catalysts was removed through a pretreatment at 300°C before STPSR. Therefore, the water can only be formed from the reaction between hydrogen and oxygen adsorbed on the catalyst. There are two possible sources for adsorbed oxygen, namely, either the product from CO dissociation, or contaminated molecular oxygen from gas phase that was not removed by hydrogen pretreatment before STPSR. In fact, the latter oxygen source can be excluded by a H₂-STPSR experiment (Fig. S8). This implies that the oxygen source of water on α-Fe catalyst can only be the dissociated O from CO. Therefore, it is concluded that CO dissociation took place at 150°C over Fe catalyst, which is also the case for Fe₅C₂ catalyst.

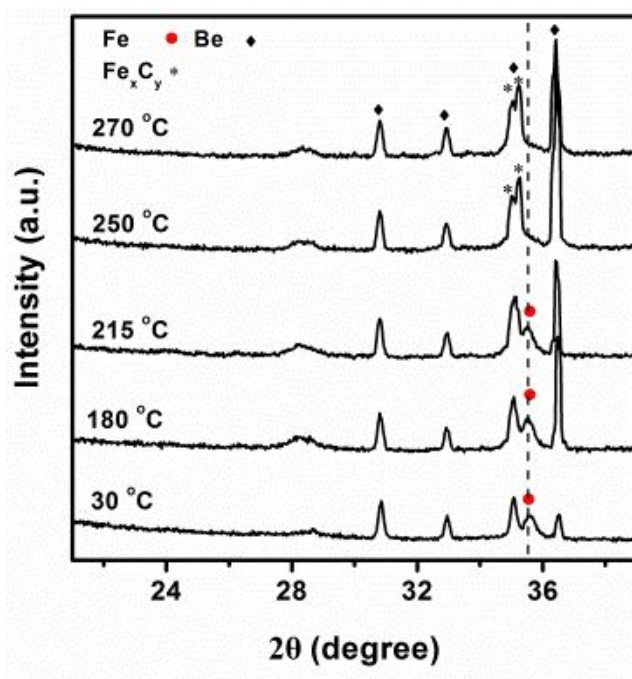


Fig. 5. In-situ XRD patterns of Fe NPs treated with 2 MPa syngas at various temperatures. (XRD was recorded in beam line 14B of Shanghai Synchrotron Facility. The diamonds mark the diffractions from beryllium-made in-situ cell).

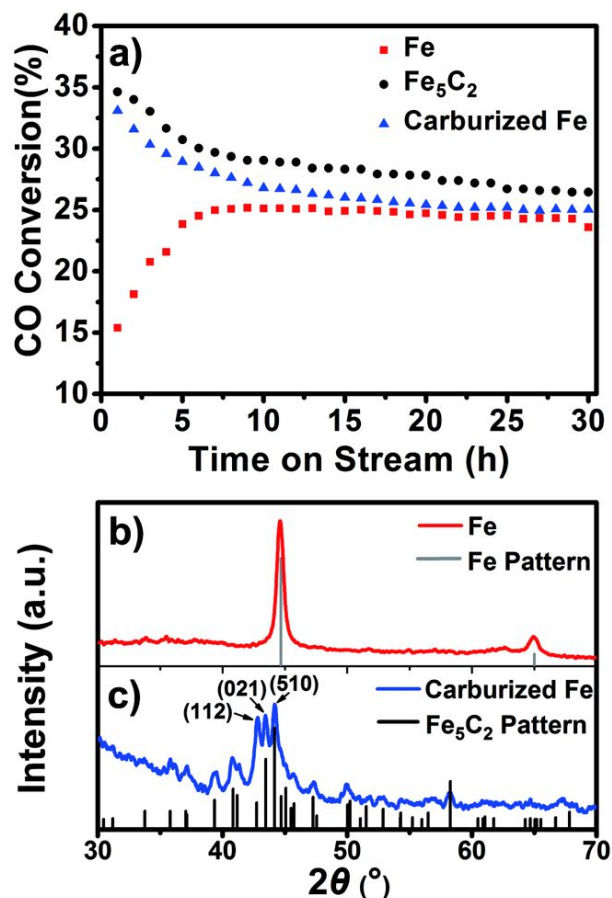


Fig. 6. (a) CO conversion of α -Fe, Fe₅C₂ and pre-carburized α -Fe NPs catalysts. XRD pattern of α -Fe NPs catalysts (b) before and (c) after carburization. It is clear that carburizing the supported α -Fe catalyst with ethylene or the mixture of ethylene and hydrogen at 350 °C for 1 hr would transform α -Fe to Fe₅C₂.

Dissociated carbon would be hydrogenated, forming subsequently the hydrocarbons.⁶²⁻⁶³ At 150 °C, the formation of the hydrocarbons was observed on Fe₅C₂, but not on α-Fe within the first 2 hrs. This implies that dissociated carbon would accumulate on α-Fe, and might diffuse into the interstitial sites of subsurface and bulk α-Fe region, carburizing α-Fe toward carbide. Fe nanoparticles can be easily carburized into iron carbides,⁶⁴ whereas the transformation from the single crystals and sheets of Fe to iron carbide is difficult⁶⁵⁻⁶⁶ which can be attributed to the difficulty for carbon atoms permeating into the interstitial sites formed by the close packing of Fe atoms. Thermodynamically, this is possible since the corresponding Gibbs free formation energy (-3.22 eV per chemical formula unit of Fe₅C₂ under FTS conditions) at this condition is exothermic (Section 8 in SI). The above hypothesis was confirmed by in-situ XRD experiments under FTS reaction condition (2 MPa syngas, Fig. 5). It can be found that under syngas stream, α-Fe, which corresponds to a diffraction with two theta value of 35.3°, was gradually transformed to iron carbides phase (two theta value of 34.8°, most like Fe₅C₂) when increasing the reaction temperature to that higher than 220 °C. Although the reaction condition is not exactly same with that in STPSR experiments, this tells compellingly that in FTS process, α-Fe is indeed apt to react with surface carbon from dissociated CO, forming iron carbide. Moreover, when we carburized the supported α-Fe catalyst with ethylene or the mixture of ethylene and hydrogen to get supported iron carbide catalyst (Fe₅C₂, as evidenced by XRD, Fig. 6b and c), we observed that the initial activity of the resulted carburized catalyst increased dramatically (Fig. 6a), reaching 33%, very close to the initial activity of pure phase Fe₅C₂ catalyst. The activity evolution of the carburized Fe catalyst almost duplicated that of Fe₅C₂ catalyst, i.e. it drops gradually in the first few hrs and becomes relatively stable after around 15 h reaction. The induction period observed on α-Fe catalyst could therefore be attributed to the process of carburization. Once the carburization was completed and Fe₅C₂ was formed, the resulted catalysts would show a higher activity because of its higher intrinsic activity of Fe₅C₂.

For the drop of activity of Fe₅C₂ catalyst with reaction time (Fig. 3), it was attributed to the oxidation of iron carbide by the oxidative products such as H₂O and CO₂ to the inactive iron oxide.

This was confirmed by the activity measurement of pure phase Fe_5C_2 treated with CO_2 at different temperature (See Fig. S9). Indeed, both the initial crystal phase of the catalyst and the reaction atmosphere could affect the structural evolution and eventually equilibrium structure of iron-based catalysts under reaction condition.

To rationalize the experimental results presented above, it is essential to study the intrinsic FTS activity of the pristine iron, and the difference with the iron carbide. Herein, DFT calculations were performed to study the crucial FTS steps including CO activation, C-C coupling and methane formation. The stepped Fe (310) and Fe-terminated Fe_5C_2 (100) surfaces (Fig. S10) were used to model the corresponding iron and iron carbides catalysts, respectively. The stepped Fe (310) was chosen here because Fe(310) surface occupies a large surface area proportion of iron Wulff shape by 22%⁶⁷ and it shows higher activity for CO dissociation as compared with the traditional (110), (100), (211) and (111) surfaces.⁶⁸ Fe_5C_2 (100) was selected here since it is one of the largest exposed surfaces under operating FTS conditions (600 K, 10 bar, $\text{H}_2/\text{CO} = 2.5$) on Fe_5C_2 Wulff construction.⁶⁹ On C-terminated Fe_5C_2 surface, there will be no active sites for CO activation or the activity of CO activation will be significant low.⁷⁰⁻⁷² Herein, in the present work, we have adopted Fe-terminated Fe_5C_2 (100) surface which stands for the C-terminated Fe_5C_2 (100) surface with abundant C vacancies, where CO dissociation is feasible.^{39, 70} Additionally, Fe(310) and Fe-terminated Fe_5C_2 (100) surfaces have the same B5 step surface and it is feasible for the direct activity and selectivity comparison between Fe and Fe_5C_2 .⁷³⁻⁷⁴ The calculated binding energetics of the important intermediates CO^* , C^* and CH^* at their most favorable sites were -2.07, -8.15 and -6.90 eV on Fe(310) while -1.91, -7.08 and -6.53 eV on Fe_5C_2 (100) (Table S2), respectively. As expected, pristine iron is more reactive than iron carbide, and the binding strength toward C^* is 1.07 eV stronger. This is determinative to the distinct activities of metal and carbide phases on CO activation, C-C coupling and methane formation.

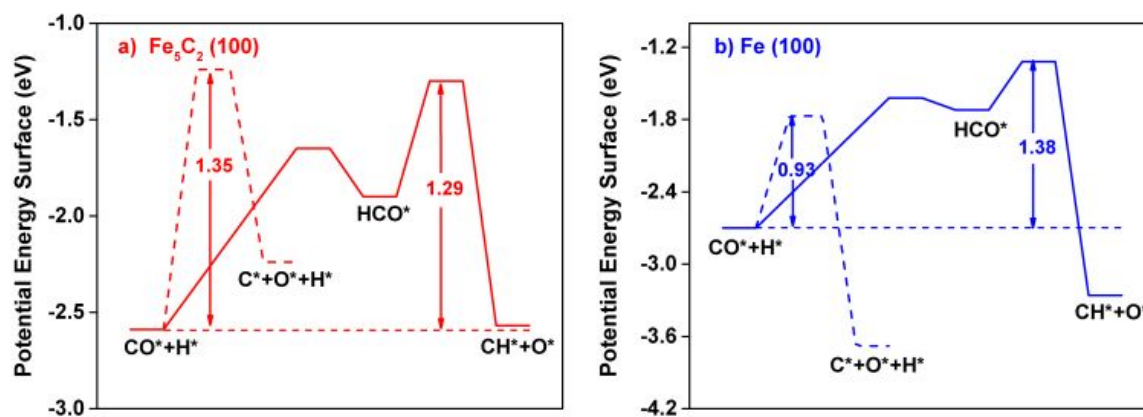


Fig. 7. The potential energy diagrams for CO dissociation on (a) Fe_5C_2 (100) (red) and (b) Fe (310) (blue) surfaces. The solid and dashed lines present direct and H-assisted CO activation pathways, respectively. The apparent activation barriers (in eV) are indicated. The corresponding geometries involved in CO activation are shown in Fig. S11 and Fig. S12.

For Fe(310), calculated E_{app} for CO dissociation was 0.93 eV, with an exothermic reaction energy (-0.98 eV) due to the strong C-Fe binding (Fig. 7a). The small barrier is in good accordance with observation of water formation at 150 °C. For C-C coupling, there are many possible pathways between CH_i and CH_j ($i, j = 0 \sim 3$). To evaluate their relative activity, equilibrium concentration of the corresponding monomers, which is proportional to their formation energy E_f (with zero energy reference of CO dissociation product), should be considered. We define accordingly apparent barrier E_{app} , namely, summation of formation energy E_f of CH_i and CH_j and their coupling barrier E_c . It is found that the strong C-Fe binding not only makes the formation of CH_i and CH_j monomers energetically highly cost with E_f falling in a magnitude of 2.49 eV, but also leads CH_i - CH_j coupling kinetically very demanding with maximum E_c of 1.99 eV (Table 2 and Fig. S15). Indeed, among all possible CH_i - CH_j coupling considered, the least E_{app} ($= E_f + E_c$) calculated was as large as 1.87 eV from C^* - CH^* coupling. Methane formation was also found highly demanding with an overall barrier of 2.27 eV (Table S3 and Fig. 8).

Table 2. Formation energy (E_f) of CH_x^* and CH_y^* , elementary coupling barrier (E_c) between CH_x^* and CH_y^* , and the apparent barrier ($E_{\text{app}} = E_f + E_c$) on Fe_5C_2 (100) and Fe (310) surfaces. The formation energy was calculated with respect to CH^* on Fe_5C_2 (100) surface and the atomic carbon C^* on the Fe (310) surface since they are located at the lowest valley of the whole potential surface.

Reaction	Fe_5C_2 (100)			Fe (310)		
	E_c (eV)	E_f (eV)	E_{app} (eV)	E_c (eV)	E_f (eV)	E_{app} (eV)
C^*-C^*	0.84	0.47	1.31	1.99	0.00	1.99
C^*-CH^*	0.78	0.24	1.02	1.45	0.42	1.87
C^*-CH_2^*	0.77	0.59	1.36	1.16	1.20	2.36
C^*-CH_3^*	1.13	0.52	1.65	1.03	1.29	2.32
CH^*-CH^*	1.02	0.00	1.02	1.38	0.85	2.23
$\text{CH}^*-\text{CH}_2^*$	0.60	0.36	0.96	1.24	1.63	2.87
$\text{CH}^*-\text{CH}_3^*$	1.19	0.28	1.47	1.35	1.71	3.06
$\text{CH}_2^*-\text{CH}_2^*$	0.48	0.72	1.20	0.79	2.41	3.20
$\text{CH}_2^*-\text{CH}_3^*$	1.16	0.64	1.80	1.07	2.49	3.56

The large barriers for C-C coupling and methane formation on Fe(310) leads the pristine iron a rather poor FTS activity. This DFT calculations are also consistent with previous experiments results that iron catalysts contain no carbide have the lowest FTS activity.²⁸ The dissociated carbon from CO would therefore stay sufficient long time on catalyst surface, which is necessary for carburization and transition toward thermodynamically more favorable carbide. As a result, the unsaturated C_2 hydrocarbon observed on iron at 170 °C (Fig. 4b) cannot come from the pristine iron. Instead, it should come from the carburized iron catalysts, namely, iron carbide. Since dissociated carbon was already available at 150 °C on the pristine iron, this also means the carburization process requires the activation temperature of 170 °C at least.

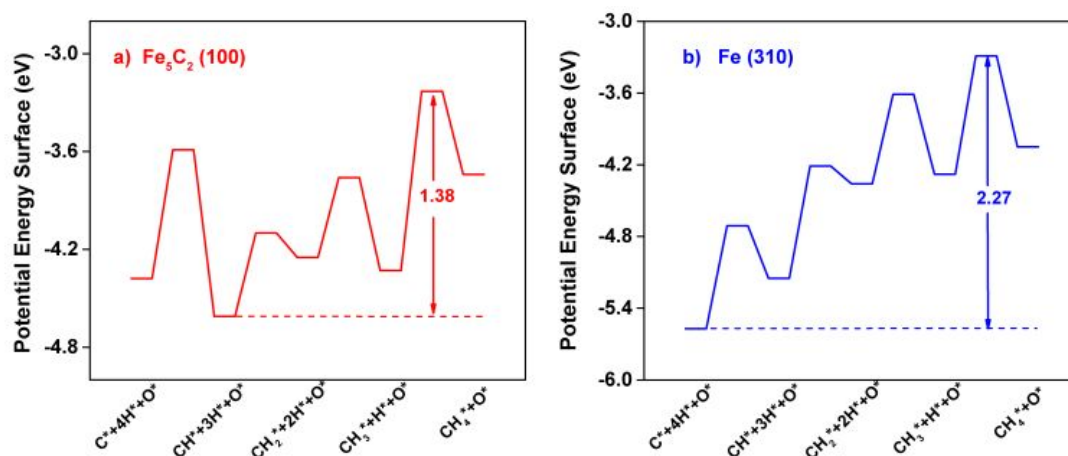


Fig. 8. The potential energy diagram for methane formation on (a) Fe₅C₂ (100) (red) and (b) Fe (310) (blue) surfaces. The apparent activation barriers (in eV) are indicated. The corresponding transition state geometries are shown in Fig. S14.

For Fe₅C₂(100), the calculated E_{app} for CO dissociation is 1.29 eV with an endothermic reaction energy (Fig. 7b), due to the destabilization of dissociated C* on carbide surface. Though CO dissociation barrier is higher than that of Fe(310), its modest value makes CO dissociation on Fe₅C₂(100) remain facile, for instance at 150 °C. This is still in accordance with experimental observation of water formation at this temperature. On the other hand, the destabilization of surface C* and CH* on carbide (Table S2) promotes greatly the C-C coupling and methane formation. The formation of CH_i and CH_j monomers become energetically much less cost with E_f falling in range of 0 ~ 0.72 eV, and the CH_i-CH_j coupling becomes kinetically facile too with maximum E_c of 1.19 eV (Table 2 and Fig. S16). As a result, the least E_{app} calculated for the C-C coupling is only 0.96 eV from CH*-CH₂* coupling. Moreover, C*-CH*, CH*-CH*, and CH₂*-CH₂* coupling are also kinetically favorable with E_{app} of 1.02, 1.02 and 1.20 eV, respectively. For methane formation, the overall barrier also decreases significantly to 1.38 eV (Table S4 and Fig. 8).

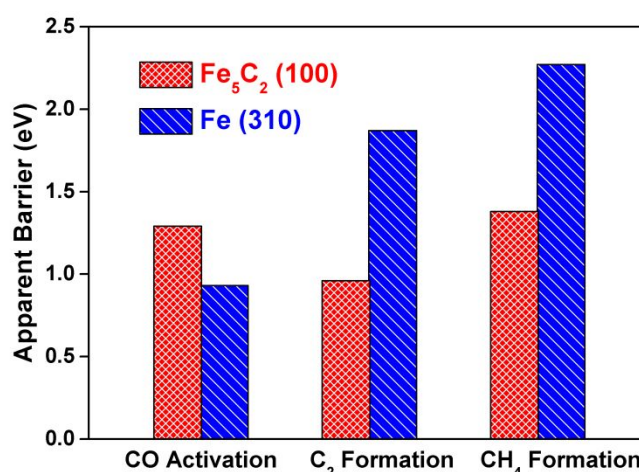


Fig. 9. Apparent barriers comparison for CO activation, C_2 and CH_4 formation on Fe_5C_2 (100) and Fe (310) surfaces.

As seen the apparent reaction barriers from Fig. 9, compared to CO activation on Fe_5C_2 (100) with barrier of 1.29 eV, the C-C coupling barriers are even lower. This means once CO dissociates on Fe_5C_2 , all these C-C coupling pathways could take place right away. This corroborates nicely the experiment over Fe_5C_2 at 150 °C (Fig. 4a), namely, once syngas were activated, both acetylene and ethylene were observed simultaneously with formation of water. Meanwhile, the barrier for methane formation remains higher than that of CO activation, a fact of that also found on Fe (310). This implies that a higher temperature for methane formation would be required, which was indeed found in corresponding STPSR experiment (Fig.4a).

Conclusion

Through a modified liquid-phase route, a series of pure-phase metallic iron and iron carbide NPs were successfully synthesized, which provided an ideal platform to investigate the fundamentals in iron-based FTS reaction that was not revealed previously. Fe_2C , Fe_7C_3 and Fe_5C_2 were all found to be active for FTS reaction, with Fe_5C_2 the most active phase. By using a house-designed STPSR method, transient information about the surface species and their reactivity were revealed. DFT calculations showed that iron carbide is intrinsically more active than the pristine iron for C-C coupling and methane

formation because of the strong binding of dissociated atomic carbon on iron. Furthermore, C-C coupling was easier compared with methane formation on iron carbide, which makes iron carbide highly active for FTS with good olefin selectivity. The distinct activities of different iron phases (metal versus carbide) revealed as well as their stability under FTS condition could be used to design more efficient iron-based FTS catalysts.

Supporting Information

Indicate that Supporting Information is included using the following statement: Supporting Information is available and includes the XRD Spectra (Fig. S1 – S2); physical absorption characterization of the support material (Fig. S3); Mössbauer effect spectra (Table S1 and Fig. S4); products distribution of catalysts (Fig. S5); TEM images and XRD patterns of used catalysts (Fig. S6 – S7); TPSR of Fe and Fe_5C_2 in pure H_2 (Fig. S8); XAFS spectra (Fig. S9) and FTS performances of CO_2 treated Fe_5C_2 catalyst; energetic and geometric information for CO activation, CH_4 formation and $\text{CH}_x\text{-CH}_x$ coupling by DFT calculations (Table S2 – S4 and Fig. S10 – S16).

Conflict of Interest (required)

There is no conflict of interest to report.

Funding Information (required)

This work was financially supported by the Natural Science Foundation of China (21725301, 91645115, 21821004, 21932002, 51631001, 91645202, 91945302), the National Key R&D Program of China (2017YFB0602200, 2017YFB0602205, 2018YFA0208603), Natural Science Foundation of Beijing Municipality (2191001) and the Chinese Academy of Sciences Key Project (QYZDJ-SSW-SLH054). XAS experiments were conducted at the Shanghai Synchrotron Radiation Facility (SSRF) and Beijing Synchrotron Radiation Facility (BSRF). XRD experiments were conducted at SSRF. The Super Computing Center of USTC is gratefully acknowledged.

References:

1. Dry, M. E., The Fischer–Tropsch (Ft) Synthesis Processes. In *Handbook of Heterogeneous Catalysis*, Wiley-VCH Verlag GmbH & Co. KGaA: 2008; Vol. 13, p 2965.
2. Remans, T. J.; Jenzer, G.; Hoek, A., Gas-to-Liquids. In *Handbook of Heterogeneous Catalysis*, Wiley-VCH Verlag GmbH & Co. KGaA: 2008; Vol. 13, p 2994.
3. de Smit, E.; Weckhuysen, B. M., The Renaissance of Iron-Based Fischer-Tropsch Synthesis: On the Multifaceted Catalyst Deactivation Behaviour. *Chem. Soc. Rev.* **2008**, *37*, 2758-2781.
4. Bukur, D. B.; Nowicki, L.; Manne, R. K.; Lang, X., Activation Studies with a Precipitated Iron Catalyst for Fischer-Tropsch Synthesis: II. Reaction Studies. *J. Catal.* **1995**, *155*, 366-375.
5. O'Brien, R. J.; Xu, L. G.; Spicer, R. L.; Davis, B. H., Activation Study of Precipitated Iron Fischer-Tropsch Catalysts. *Energy Fuels* **1996**, *10*, 921-926.
6. Bukur, D. B.; Okabe, K.; Rosynek, M. P.; Li, C.; Wang, D.; Rao, K.; Huffman, G., Activation Studies with a Precipitated Iron Catalyst for Fischer-Tropsch Synthesis: I. Characterization Studies. *J. Catal.* **1995**, *155*, 353-365.
7. Shroff, M. D.; Kalakkad, D. S.; Coulter, K. E.; Kohler, S. D.; Harrington, M. S.; Jackson, N. B.; Sault, A. G.; Datye, A. K., Activation of Precipitated Iron Fischer-Tropsch Synthesis Catalysts. *J. Catal.* **1995**, *156*, 185-207.
8. Eliason, S.; Bartholomew, C., Reaction and Deactivation Kinetics for Fischer–Tropsch Synthesis on Unpromoted and Potassium-Promoted Iron Catalysts. *Appl. Catal. A: Gen.* **1999**, *186*, 229-243.
9. Moyer, M. M.; Karakaya, C.; Kee, R. J.; Trewyn, B. G., In Situ Formation of Metal Carbide Catalysts. *ChemCatChem* **2017**, *9*, 3090-3101.
10. Yang, X.; Zhang, H.; Liu, Y.; Ning, W.; Han, W.; Liu, H.; Huo, C., Preparation of Iron Carbides Formed by Iron Oxalate Carburization for Fischer–Tropsch Synthesis. *Catalysts* **2019**, *9*, 347.
11. Liaw, S. J.; Davis, B. H., Fischer-Tropsch Synthesis. Compositional Changes in an Iron Catalyst During Activation and Use. *Top. Catal.* **2000**, *10*, 133-139.
12. Li, S. Z.; Meitzner, G. D.; Iglesia, E., Structure and Site Evolution of Iron Oxide Catalyst Precursors During the Fischer-Tropsch Synthesis. *J. Phys. Chem. B* **2001**, *105*, 5743-5750.
13. Perez-Alonso, F. J.; Herranz, T.; Rojas, S.; Ojeda, M.; Lopez Granados, M.; Terreros, P.; Fierro, J. L. G.; Gracia, M.; Gancedo, J. R., Evolution of the Bulk Structure and Surface Species on Fe-Ce Catalysts During the Fischer-Tropsch Synthesis. *Green Chem.* **2007**, *9*, 663-670.
14. de Smit, E.; Swart, I.; Creemer, J. F.; Hoveling, G. H.; Gilles, M. K.; Tyliszczak, T.; Kooyman, P. J.; Zandbergen, H. W.; Morin, C.; Weckhuysen, B. M., Nanoscale Chemical Imaging of a Working Catalyst by Scanning Transmission X-Ray Microscopy. *Nature* **2008**, *456*, 222-225.

15. Janbroers, S.; Louwen, J. N.; Zandbergen, H. W.; Kooyman, P. J., Insights into the Nature of Iron-Based Fischer-Tropsch Catalysts from Quasi in Situ Tem-EELS and XRD. *J. Catal.* **2009**, *268*, 235-242.
16. Fjellvag, H.; Karen, P., Crystal-Structure of Magnesium Sesquicarbide. *Inorg. Chem.* **1992**, *31*, 3260-3263.
17. Ferrari, A. C.; Meyer, J.; Scardaci, V.; Casiraghi, C.; Lazzeri, M.; Mauri, F.; Piscanec, S.; Jiang, D.; Novoselov, K.; Roth, S., Raman Spectrum of Graphene and Graphene Layers. *Phys. Rev. Lett.* **2006**, *97*, 187401.
18. Sun, L. D.; Jia, C. J.; Luo, F.; Han, X. D.; Heyderman, L. J.; Yan, Z. G.; Yan, C. H.; Zheng, K.; Zhang, Z.; Takano, M.; Hayashi, N.; Eltschka, M.; Klau, M.; Rudiger, U.; Kasama, T.; Cervera-Gontard, L.; Dunin-Borkowski, R. E.; Tzvetkov, G.; Raabe, J., Large-Scale Synthesis of Single-Crystalline Iron Oxide Magnetic Nanorings. *J. Am. Chem. Soc.* **2008**, *130*, 16968-16977.
19. Yang, C.; Zhao, H. B.; Hou, Y. L.; Ma, D., Fe₅C₂ Nanoparticles: A Facile Bromide-Induced Synthesis and as an Active Phase for Fischer-Tropsch Synthesis. *J. Am. Chem. Soc.* **2012**, *134*, 15814-15821.
20. Liu, X.-W.; Cao, Z.; Zhao, S.; Gao, R.; Meng, Y.; Zhu, J.-X.; Rogers, C.; Huo, C.-F.; Yang, Y.; Li, Y.-W., Iron Carbides in Fischer-Tropsch Synthesis: Theoretical and Experimental Understanding in Epsilon-Iron Carbide Phase Assignment. *J. Phys. Chem. C* **2017**, *121*, 21390-21396.
21. Wezendonk, T. A.; Sun, X.; Dugulan, A. I.; van Hoof, A. J.; Hensen, E. J.; Kapteijn, F.; Gascon, J., Controlled Formation of Iron Carbides and Their Performance in Fischer-Tropsch Synthesis. *J. Catal.* **2018**, *362*, 106-117.
22. Wang, P.; Chen, W.; Chiang, F.-K.; Dugulan, A. I.; Song, Y.; Pestman, R.; Zhang, K.; Yao, J.; Feng, B.; Miao, P., Synthesis of Stable and Low-CO₂ Selective E-Iron Carbide Fischer-Tropsch Catalysts. *Sci. Adv.* **2018**, *4*, eaau2947.
23. Kuei, C.-K.; Lee, M.-D., Temperature-Programmed Reaction of Pre-Adsorbed CO on Iron Catalyst: New Experimental Evidence for Competition Model. *J. Mol. Catal.* **1991**, *65*, 293-305.
24. Niemantsverdriet, J.; Van der Kraan, A.; Van Dijk, W.; Van der Baan, H., Behavior of Metallic Iron Catalysts During Fischer-Tropsch Synthesis Studied with Mossbauer Spectroscopy, X-Ray Diffraction, Carbon Content Determination, and Reaction Kinetic Measurements. *J. Phys. Chem.* **2002**, *84*, 3363-3370.
25. Amelse, J. A.; Butt, J. B.; Schwartz, L. H., Carburization of Supported Iron Synthesis Catalysts. *J. Phys. Chem.* **1978**, *82*, 558-563.
26. Rao, K. R. P. M.; Huggins, F. E.; Ganguly, B.; Mahajan, V.; Huffman, G. P.; Davis, B.; O'Brien, R. J.; Xu, L. G.; Rao, V. U. S., Effect of Pre-Heat Treatment on a Fischer-Tropsch Iron Catalyst. *Hyperfine Interact.* **1994**, *93*, 1755-1758.

27. Badani, M. V.; Delgass, W. N., The Active Phase of Iron Catalysts for Acetonitrile Synthesis. *J. Catal.* **1999**, *187*, 506-517.
28. Mansker, L. D.; Jin, Y.; Bukur, D. B.; Datye, A. K., Characterization of Slurry Phase Iron Catalysts for Fischer–Tropsch Synthesis. *Appl. Catal. A: Gen.* **1999**, *186*, 277-296.
29. Schulz, H.; Riedel, T.; Schaub, G., Fischer-Tropsch Principles of CO-Hydrogenation on Iron Catalysts. *Top. Catal.* **2005**, *32*, 117-124.
30. Herranz, T.; Rojas, S.; Perez-Alonso, F. J.; Ojeda, M.; Terreros, P.; Fierro, J. L. G., Genesis of Iron Carbides and Their Role in the Synthesis of Hydrocarbons from Synthesis Gas. *J. Catal.* **2006**, *243*, 199-211.
31. Hao, Q. L.; Bai, L.; Xiang, H. W.; Li, Y. W., Phase Transformations of a Spray-Dried Iron Catalyst for Slurry Fischer-Tropsch Synthesis During Activation and Reaction. *Fuel Process. Technol.* **2008**, *89*, 1358-1364.
32. de Smit, E.; Cinquini, F.; Beale, A. M.; Safonova, O. V.; van Beek, W.; Sautet, P.; Weckhuysen, B. M., Stability and Reactivity of Epsilon-Chi-Theta Iron Carbide Catalyst Phases in Fischer-Tropsch Synthesis: Controlling $\mu(\text{C})$. *J. Am. Chem. Soc.* **2010**, *132*, 14928-14941.
33. Torres Galvis, H. M.; Bitter, J. H.; Khare, C. B.; Ruitenbeek, M.; Dugulan, A. I.; de Jong, K. P., Supported Iron Nanoparticles as Catalysts for Sustainable Production of Lower Olefins. *Science* **2012**, *335*, 835-838.
34. Yang, C.; Zhao, B.; Gao, R.; Yao, S.; Zhai, P.; Li, S.; Yu, J.; Hou, Y.; Ma, D., Construction of Synergistic $\text{Fe}_5\text{C}_2/\text{Co}$ Heterostructured Nanoparticles as an Enhanced Low Temperature Fischer–Tropsch Synthesis Catalyst. *ACS Catal.* **2017**, *7*, 5661-5667.
35. Gao, R.; Liu, X.; Cao, Z.; Liu, X.-W.; Lu, K.; Ma, D.; Yang, Y.; Li, Y.-W.; Hoffmann, R.; Wen, X.-D., Carbon Permeation: The Prerequisite Elementary Step in Iron-Catalyzed Fischer–Tropsch Synthesis. *Catal. Lett.* **2019**, *149*, 645-664.
36. Chang, Q.; Zhang, C.; Liu, C.; Wei, Y.; Cheruvathur, A. V.; Dugulan, A. I.; Niemantsverdriet, J.; Liu, X.; He, Y.; Qing, M., Relationship between Iron Carbide Phases ($\epsilon\text{-Fe}_2\text{C}$, Fe_7C_3 , and $\text{X-Fe}_5\text{C}_2$) and Catalytic Performances of Fe/SiO_2 Fischer–Tropsch Catalysts. *ACS Catal.* **2018**, *8*, 3304-3316.
37. Lu, F.; Chen, X.; Lei, Z.; Wen, L.; Zhang, Y., Revealing the Activity of Different Iron Carbides for Fischer-Tropsch Synthesis. *Appl. Catal., B* **2020**, 119521.
38. Zhuo, O.; Yang, L.; Gao, F.; Xu, B.; Wu, Q.; Fan, Y.; Zhang, Y.; Jiang, Y.; Huang, R.; Wang, X.; Hu, Z., Stabilizing the Active Phase of Iron-Based Fischer–Tropsch Catalysts for Lower Olefins: Mechanism and Strategy. *Chem. Sci.* **2019**, *10*, 6083-6090.
39. Huo, C.-F.; Li, Y.-W.; Wang, J.; Jiao, H., Insight into CH_4 Formation in Iron-Catalyzed Fischer–Tropsch Synthesis. *J. Am. Chem. Soc.* **2009**, *131*, 14713-14721.
40. Cheng, J.; Hu, P.; Ellis, P.; French, S.; Kelly, G.; Lok, C. M., An Energy Descriptor to Quantify

Methane Selectivity in Fischer-Tropsch Synthesis: A Density Functional Theory Study. *J. Phys. Chem. C* **2009**, *113*, 8858-8863.

41. Ojeda, M.; Nabar, R.; Nilekar, A. U.; Ishikawa, A.; Mavrikakis, M.; Iglesia, E., CO Activation Pathways and the Mechanism of Fischer-Tropsch Synthesis. *J. Catal.* **2010**, *272*, 287-297.

42. Shetty, S. G.; Ciobica, I. M.; Hensen, E. J. M.; van Santen, R. A., Site Regeneration in the Fischer-Tropsch Synthesis Reaction: A Synchronized CO Dissociation and C-C Coupling Pathway. *Chem. Commun.* **2011**, *47*, 9822-9824.

43. Pham, T. H.; Duan, X.; Qian, G.; Zhou, X.; Chen, D., Co Activation Pathways of Fischer-Tropsch Synthesis on X-Fe₅C₂ (510): Direct Versus Hydrogen-Assisted CO Dissociation. *J. Phys. Chem. C* **2014**, *118*, 10170-10176.

44. Chen, W.; Filot, I. A.; Pestman, R.; Hensen, E. J., Mechanism of Cobalt-Catalyzed CO Hydrogenation: 2. Fischer-Tropsch Synthesis. *ACS Catal.* **2017**, *7*, 8061-8071.

45. Rivera de la Cruz, J. G.; Sabbe, M. K.; Reyniers, M.-F., First Principle Study on the Adsorption of Hydrocarbon Chains Involved in Fischer-Tropsch Synthesis over Iron Carbides. *J. Phys. Chem. C* **2017**, *121*, 25052-25063.

46. Kresse, G.; Hafner, J., Ab Initio Molecular Dynamics for Liquid Metals. *Phys. Rev. B* **1993**, *47*, 558.

47. Kresse, G.; Furthmüller, J., Efficient Iterative Schemes for Ab Initio Total-Energy Calculations Using a Plane-Wave Basis Set. *Phys. Rev. B* **1996**, *54*, 11169.

48. Kresse, G.; Joubert, D., From Ultrasoft Pseudopotentials to the Projector Augmented-Wave Method. *Phys. Rev. B* **1999**, *59*, 1758.

49. Perdew, J. P.; Burke, K.; Ernzerhof, M., Generalized Gradient Approximation Made Simple. *Phys. Rev. Lett.* **1996**, *77*, 3865-3868.

50. Monkhorst, H. J.; Pack, J. D., Special Points for Brillouin-Zone Integrations. *Phys. Rev. B* **1976**, *13*, 5188-5192.

51. Retief, J. J., Powder Diffraction Data and Rietveld Refinement of Hägg-Carbide, X-Fe₅C₂. *Powder Diffr.* **1999**, *14*, 130-132.

52. Kittel, C.; McEuen, P., *Introduction to Solid State Physics*; Wiley New York, 1996; Vol. 8.

53. Sun, K.; Zhao, Y.; Su, H. Y.; Li, W. X., Force Reversed Method for Locating Transition States. *Theor. Chem. Acc.* **2012**, *131*, 1-10.

54. Henkelman, G.; Uberuaga, B. P.; Jónsson, H., A Climbing Image Nudged Elastic Band Method for Finding Saddle Points and Minimum Energy Paths. *J. Chem. Phys.* **2000**, *113*, 9901.

55. Yu, G.; Sun, B.; Pei, Y.; Xie, S.; Yan, S.; Qiao, M.; Fan, K.; Zhang, X.; Zong, B., Fe_xO_y@ C Spheres as an Excellent Catalyst for Fischer-Tropsch Synthesis. *J. Am. Chem. Soc.* **2010**, *132*, 935-937.

56. van Steen, E.; Claeys, M., Fischer -Tropsch Catalysts for the Biomass -to -Liquid (BTL) - Process. *Chem. Eng. Technol.* **2008**, *31*, 655-666.
57. Chen, W.; Fan, Z.; Pan, X.; Bao, X., Effect of Confinement in Carbon Nanotubes on the Activity of Fischer- Tropsch Iron Catalyst. *J. Am. Chem. Soc.* **2008**, *130*, 9414-9419.
58. Santos, V. P.; Wezendonk, T. A.; Jaén, J. J. D.; Dugulan, A. I.; Nasalevich, M. A.; Islam, H.-U.; Chojecki, A.; Sartipi, S.; Sun, X.; Hakeem, A. A., Metal Organic Framework-Mediated Synthesis of Highly Active and Stable Fischer-Tropsch Catalysts. *Nat. Commun.* **2015**, *6*, 6451.
59. Xu, K.; Sun, B.; Lin, J.; Wen, W.; Pei, Y.; Yan, S.; Qiao, M.; Zhang, X.; Zong, B., ϵ -Iron Carbide as a Low-Temperature Fischer-Tropsch Synthesis Catalyst. *Nat. Commun.* **2014**, *5*, 1-8.
60. Ma, D.; Shu, Y. Y.; Cheng, M. J.; Xu, Y. D.; Bao, X. H., On the Induction Period of Methane Aromatization over Mo-Based Catalysts. *J. Catal.* **2000**, *194*, 105-114.
61. Ma, D.; Wang, D.; Su, L.; Shu, Y.; Xu, Y.; Bao, X., Carbonaceous Deposition on Mo/HMCM-22 Catalysts for Methane Aromatization: A Tp Technique Investigation. *J. Catal.* **2002**, *208*, 260-269.
62. van Santen, R. A.; Ciobica, I. M.; van Steen, E.; Ghouri, M. M., Mechanistic Issues in Fischer-Tropsch Catalysis. *Adv. Catal.* **2011**, *54*, 127-187.
63. Van Santen, R.; Markvoort, A.; Filot, I.; Ghouri, M.; Hensen, E., Mechanism and Microkinetics of the Fischer-Tropsch Reaction. *Phys. Chem. Chem. Phys.* **2013**, *15*, 17038-17063.
64. Zhou, X.; Mannie, G. J. A.; Yin, J.; Yu, X.; Weststrate, C. J.; Wen, X.; Wu, K.; Yang, Y.; Li, Y.; Niemantsverdriet, J. W., Iron Carbide on Thin-Film Silica and Silicon: A near-Ambient-Pressure X-Ray Photoelectron Spectroscopy and Scanning Tunneling Microscopy Study. *ACS Catal.* **2018**, *8*, 7326-7333.
65. Erley, W.; McBreen, P. H.; Ibach, H., Evidence for CH_x Surface Species after the Hydrogenation of CO over an Fe(110) Single Crystal Surface. *J. Catal.* **1983**, *84*, 229-234.
66. Hwang, H.-S.; Chung, U.-C.; Chung, W.-S.; Cho, Y.-R.; Jung, B.-H.; Martin, G. P., Carburization of Iron Using CO-H₂ Gas Mixture. *Met. and Mater. Int.* **2004**, *10*, 77-82.
67. Huo, C.-F.; Wu, B.-S.; Gao, P.; Yang, Y.; Li, Y.-W.; Jiao, H., The Mechanism of Potassium Promoter: Enhancing the Stability of Active Surfaces. *Angew. Chem. Int. Ed.* **2011**, *50*, 7403-7406.
68. Sorescu, D. C., Plane-Wave Dft Investigations of the Adsorption, Diffusion, and Activation of CO on Kinked Fe(710) and Fe(310) Surfaces. *J. Phys. Chem. C* **2008**, *112*, 10472-10489.
69. Zhao, S.; Liu, X.-W.; Huo, C.-F.; Li, Y.-W.; Wang, J.; Jiao, H., Surface Morphology of Hägg Iron Carbide (X-Fe₅C₂) from Ab Initio Atomistic Thermodynamics. *J. Catal.* **2012**, *294*, 47-53.
70. Ozbek, M. O.; Niemantsverdriet, J. W., Elementary Reactions of CO and H₂ on C-Terminated X-Fe₅C₂(001) Surfaces. *J. Catal.* **2014**, *317*, 158-166.
71. Broos, R. J. P.; Zijlstra, B.; Filot, I. A. W.; Hensen, E. J. M., Quantum-Chemical DFT Study of

Direct and H- and C-Assisted CO Dissociation on the X-Fe₅C₂ Hägg Carbide. *J. Phys. Chem. C* **2018**, *122*, 9929-9938.

72. Li, T.; Wen, X.; Yang, Y.; Li, Y.-W.; Jiao, H., Mechanistic Aspects of CO Activation and C–C Bond Formation on the Fe/C- and Fe-Terminated Fe₃C(010) Surfaces. *ACS Catal.* **2020**, *10*, 877-890.

73. Cao, D.-B.; Zhang, F.-Q.; Li, Y.-W.; Jiao, H., Density Functional Theory Study of CO Adsorption on Fe₅C₂(001), -(100), and -(110) Surfaces. *J. Phys. Chem. B* **2004**, *108*, 9094-9104.

74. Elahifard, M. R.; Pérez Jigato, M.; Niemantsverdriet, J. W., Ab-Initio Calculations of the Direct and Hydrogen-Assisted Dissociation of CO on Fe(310). *Chem. Phys. Lett.* **2012**, *534*, 54-57.

Table of Contents Graphic (required)

